A hierarchically porous Fe-N-C synthesized by dual melt-salt-mediated template as advanced electrocatalyst for efficient oxygen reduction in zinc-air battery

Hao Xu [a], Dan Wang [a], Peixia Yang [a,*], Lei Du [a,b,**], Xiangyu Lu [a], Ruopeng Li [a], Lilai Liu [c], Jinqiu Zhang [a], Maozhong An [a]

[a] MIIT Key Laboratory of Critical Materials Technology for New Energy Conversion and Storage, School of Chemistry and Chemical Engineering, Harbin Institute of Technology, 150001 Harbin, China
[b] School of Chemistry and Chemical Engineering, Huangpu Hydrogen Innovation Center, Guangzhou Key Laboratory for Clean Energy and Materials, Guangzhou University, 510006 Guangzhou, China
[c] College of Environmental and Chemical Engineering, Heilongjiang University of Science and Technology, Harbin 150022, China

ARTICLE INFO

ABSTRACT

The reasonable design of porous structures is important but usually overlooked for nonprecious metal ORR catalysts. In this study, a facile dual melt-salt-mediated templating method is developed to prepare a Fe-N-C catalyst with tailored porous framework. The ZnCl$_2$ and NaCl are employed to construct abundant micropores and promote the transformation of partial micropores to mesopores, respectively, reasonably forming a 3D hierarchically porous framework. The catalyst demonstrates a satisfactory surface area (1605 m^2/g), promoting mass transport and exposure of FeN$_4$ sites. Interestingly, the dual melt-salt templates avoid rapid loss of nitrogen during pyrolysis, thus enhancing Fe-N$_4$ active center density. Therefore, the obtained Fe-N-C material presents outstanding ORR performance in both alkaline and acid media, as well as good stability. The advances of this catalyst are further proved in liquid and solid-state Zn-air battery, with nice discharge stability and high peak power densities.

1. Introduction

Zn-air batteries (ZABs) have been attracting enormous research interests as a sustainable, efficient and clean energy device [1–5]. The effective catalyst toward ORR is critical for the deployment of ZABs [6–8]. Particularly, benchmark platinum-based ORR catalysts are desired to be replaced with advanced non-noble metal materials to decrease the expense [9–13].

In various non-noble metal catalysts, Fe-N-C material is one of the most hopeful candidates because of its superior catalytic durability and performance [14–18]. The most widely used synthetic method for Fe-N-C material is thermal treatment of Fe- and N-containing precursors [19,20]. However, the pyrolysis process cannot accurately control the formation of Fe-N$_x$ moieties—Fe tends to agglomerate and form Fe nanoparticles, lowering the activity and blocking the transport channels

[21,22]. In addition, the Fe-N-C catalyst usually has only many micropores, resulting in increased transport resistance for reactants and products [23]. Therefore, it is necessary to avoid inactive Fe nanoparticles and open porous structures for mass transport. To achieve these goals, the hierarchically meso-/microporous structure is helpful, [9,23,24] not only promoting the mass transport, but also increasing the affinity and accommodation (high surface area) for the active Fe-N$_x$ sites [25–27]. It is difficult but significative to prepare the Fe-N-C with hierarchically porous framework for ORR.

The template assisted methods are promising in tailoring hierarchically porous carbon-based catalysts for ORR. For instance, Zhu et al. [28] used SiO$_2$ and ZnCl$_2$ as templates to synthesis the Fe-N-C catalyst. After removing SiO$_2$ templates, mesopores were introduced. However, this process needs toxic acid solution, which sets barrier for large-scale preparation [1,29,30]. Recently, NaCl has been emerging as an effective

template to control mesoporous structure [23,31,32]. Particularly, NaCl is easy to remove by washing and can be recycled via a recrystallization process, which makes the preparation cost-effective and environmentally friendly [20,33]. Nevertheless, the mesopore formation mechanism using NaCl template is still controversial, which needs further study [34].

On the other hand, the molten-salt can act as a protective agent that prevents the catalyst from nitrogen elimination and structure collapse during pyrolysis [30,35]. Wei and co-workers [30,36] confirmed that $ZnCl_2$ molten-salt increased the content of nitrogen and Fe-N_x species in the prepared catalysts. The NaCl molten-salt has the similar effect [33]. Even so, the N dopant content is usually below 5 at% by using the single molten salt template.

Herein, we report a facile and general dual melt-salt-mediated templating method to produce the hierarchically porous nitrogen-doped carbon (HPNC) and then the Fe-N-C (HPFe-N-C) materials. The low-cost $ZnCl_2$ and NaCl as molten-salt templates help fabricating high-surface-area micro-/mesoporous nanostructure (1605 m^2/g) and keep high N dopant content (5.21 at%) during pyrolysis. Interestingly, the NaCl template can promote partial micropores to merge and form mesopores. The confinement effect of HPNC and its strong affinity with Fe-1, 10-phenanthroline (Phen) complex prevent the appearance of inactive iron-nanoparticles. The optimized HPFe-N-C material presents high ORR activity and stability in alkaline media with a half-wave potential ($E_{1/2}$) of 0.911 V, as well as good acidic catalytic performance ($E_{1/2}$ =0.802 V). Impressively, both the aqueous ZABs and solid ZABs using HPFe-N-C catalyst as the air cathodes show better peak power density and higher stability than ZABs using platinum/carbon.

2. Experimental section

2.1. Catalyst preparation

2.1.1. Synthesis of the hierarchically porous N-doped carbon (HPNC)

The HPNC was synthesized by pyrolyzing a mixed precursor. Briefly, the dual templates consisting of $ZnCl_2$ (4 g, 29.34 mmol) and NaCl (4 g, 68.45 mmol) were mixed together with adenine (0.8 g, 5.92 mmol) followed by grounding in an agate mortar. Then, the precursor was annealed at 900 °C for 1 h in H$_2$/Ar (5%: 95%) gas with 5 °C min^{-1}. When the temperature of tube furnace dropped to the normal temperature, the prepared HPNC material was treated by 1 M HCl and deionized water for four times and dried at 60 °C for 13 h.

2.1.2. Synthesis of the hierarchically porous iron/nitrogen co-doped carbon (HPFe-N-C)

The HPFe-N-C catalyst was synthesized using the as-prepared HPNC. FeCl$_2$ (5 mg) and 1, 10-phenanthroline (Phen, 20 mg) were dissolved into a solution (15 mL) consisting of H$_2$O and C$_2$H$_5$OH to generate the Fe-Phen complex at room temperature. Then, the HPNC (85 mg) was added in the prepared Fe-Phen solution and then stirried for 13 h at 60 °C. The above mixture was then frozen and dried at − 45 °C for 12 h. After that, HPFe-N-C material was synthesized by heating the above mixture at 800 °C for 2 h in H$_2$/Ar (5%: 95%) gas with 5 °C min^{-1}. In contrast, reference Fe-N-C@ZnCl$_2$ and Fe-N-C@NaCl materials were prepared using similar process with the HPFe-N-C except for adding single $ZnCl_2$ and NaCl as the template. The reference Fe-N-C material was synthesized using alike procedures (to HPFe-N-C) without using $ZnCl_2$ and NaCl template.

2.2. Physicochemical characterizations

The morphology was observed by scanning electron microscope (SEM, HITACHI SU8010) and transmission electron microscope (TEM, JEOL 2100). The spherical aberration corrected TEM image was collected using FEI Theims Z. The Raman spectra (HR800) and X-ray diffraction (XRD, Bruker D8 diffractometer) patterns were employed to analyze the defect level and crystal structure, respectively. The N$_2$ adsorption-desorption analysis was conducted on a 3H-2000PS1 analyzer. The results of inductively coupled plasma optical emission spectrometry (ICP-OES) and X-ray photoelectron spectroscopy (XPS) were obtained from Agilent 7700 and Physical Electronics PHI 5700 instrument, respectively. X-ray absorption spectra (Fe K-edge) analysis was obtained on the BL14W1 station at the Shanghai Synchrotron Radiation Facility.

2.3. Electrochemical measurements

Electrochemical measurements were carried out at room temperature in the standard three-electrode system. The electrochemical workstation was CHI 760E. The working electrode was glassy carbon rotating disk electrode. In 0.1 M KOH solution, the reference electrode and counter electrode was Hg/HgO electrode and graphite sheet, respectively. In 0.1 M HClO$_4$ solution, the reference electrode and counter electrode was Hg/Hg$_2$SO$_4$ electrode and Pt foil, respectively. The catalyst ink was synthesized as follows: 2.5 mg catalyst was dispersed in the solution consisting of 20 μL Nafion, 300 μL ultrapure water, and 180 μL isopropanol. Then, the as-prepared catalysts ink was coated on the working electrode for further tests in 0.1 M KOH (0.459 mg cm^{-2}) and 0.1 M HClO$_4$ (0.6 mg cm^{-2}). For comparison, the performance of commercial Pt/C (20 wt%) was also tested in both alkaline and acid media, with a fixed loading of 0.255 mg cm^{-2}. The potentials mentioned in this work are relative to the reversible hydrogen electrode (RHE).

The transferred electron number (n) and specific kinetic current density for ORR were calculated by using the Koutecky-Levich (K-L) equation, the detailed equation and corresponding calculation process can be found in our previous works [27]. The rotating ring-disk electrode (RRDE) measurements were used to calculate the hydrogen peroxide yield and n.

2.4. Zn-air batteries test

The liquid ZAB used the treated Zn foil and the Ni foam coated with catalyst ink (2 mg cm^{-2}) as anode and cathode, respectively. The ink was synthesized by dispersing 2.5 mg HPFe-N-C, 4 mg activated carbon and 1 mg acetylene black in the mixed solution consisting of 200 μL isopropyl alcohol and 8 μL Nafion. A waterproof breathable film was chosen as the backing layer for the Ni foam. For comparison, Pt/C-based air cathode (2 mg cm^{-2}) was prepared by the same method. The electrolyte in primary aqueous Zn-air batteries is 6 M KOH solution. The polarization curve was conducted using CHI 760E workstation at room temperature. The galvanostatic discharge test was performed with the Land CT2001A system. Zn-Air batteries were tested using the self-breathing air electrode configuration. For the Zn electrode, a mini pump was employed to drive electrolyte through at a flow rate of 10 mL/ min, which reduced the polarization in the reaction process.

The solid ZAB used the treated Zn foil and the Ni foam coated with catalyst ink (2 mg cm^{-2}) as anode and cathode, respectively. The solid-state electrolyte PVA polymer was synthesized as follows: the specified amounts of PVA, Zn(CH$_3$COO)$_2$ and KOH were dispersed in fifty mL aqueous solution followed by stirring for forty minutes at ninety-five °C. Then the gel polymer was poured onto a glass plate and froze at zero °C for six hours. The solid-state electrolyte was obtained after keeping at room temperature for twelve hours.

2.5. Density functional theory calculations

The theoretical calculations were conducted employing the Dmol^3 module in the Materials Studio. The generalized gradient approximation (GGA) with Perdew-Burke-Ernzerhof (PBE) functional was selected to represent the electronic exchange-correlation. The DNP method was selected as basis set. The detailed parameter setting is consistent with our previous works [27].
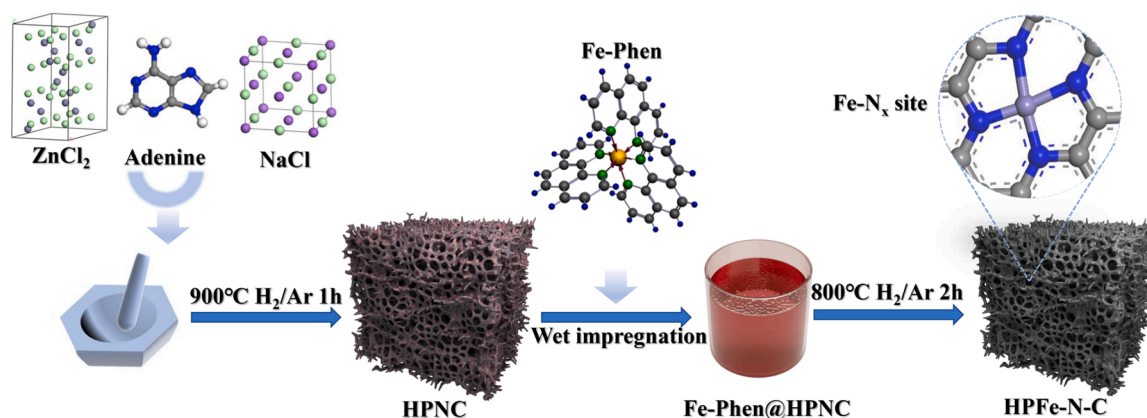
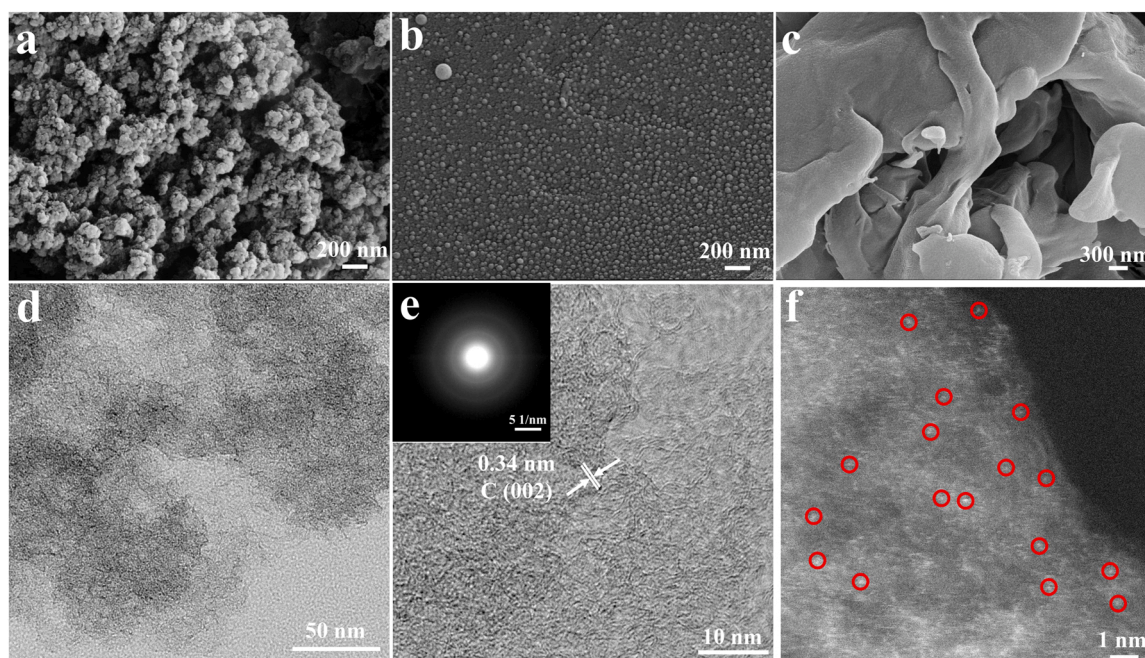**Scheme 1.** The preparation flow for HPNC and HPFe-N-C.

Fig. 1. SEM images of (a) HPFe-N-C, (b) Fe-N-C@ZnCl$_2$ and (c) Fe-N-C@NaCl. (d) TEM images and (e) HRTEM images of HPFe-N-C. (f) The spherical aberration corrected TEM image of HPFe-N-C.

3. Results and discussion

3.1. Physical characterizations

The preparation flow of HPNC and HPFe-N-C catalyst is revealed in Scheme 1. The HPNC support is synthesized via pyrolyzing adenine with the dual melt-salt templates, i.e., NaCl and ZnCl$_2$. The adenine is chosen as the nitrogen source on account of its low-cost and high N content. It is interesting that the yield of carbon is pretty low if no NaCl and ZnCl$_2$ templates are employed (see in Fig. S1), suggesting that the majority of adenine precursor (without templates) is lost during pyrolysis. Impressively, by using templates, the well-defined HPNC is obtained, having more retained material (see in Fig. S1). Above results suggest that, under the protection of molten salt templates, the adenine with low decomposition temperature (below 400 °C) [35] was transformed into N-rich HPNC during pyrolysis, instead of direct decomposition.

To synthesize the HPFe-N-C catalyst, Fe-Phen complex is introduced into the HPNC by wet impregnation. The Phen as a space isolation agent can effectively avoid the formation of inactive iron nanoparticles. Reasonably, after the pyrolysis at 800 °C under H$_2$/Ar surroundings,

hierarchically porous Fe-N-C electrocatalysts are generated. To analyze the detailed microstructure, the synthesized materials are observed by SEM. By employing dual ZnCl$_2$ and NaCl as templates, a caviar-like three-dimensional hierarchically porous framework with abundant irregular polyhedron is generated in the HPFe-N-C (Fig. 1a). In contrast, without NaCl template, the Fe-N-C@ZnCl$_2$ sample presents a sheet structure with no obvious mesopores or macropores (Fig. 1b). While a blocky structure with irregular large pores (> 300 nm) is seen in the Fe-N-C@NaCl (Fig. 1c). This suggests that, without dual templates, the hierarchically porous structure cannot form in the final catalyst. For the dual template approach, ZnCl$_2$ can be evaporated at high temperature during HPNC synthesis to form abundant micropore framework as well as high specific surface area, which can be regarded as a micropore creator in this work. After removing NaCl by washing, abundant mesopores are retained in the synthesized material.

Details of HPFe-N-C catalyst are presented in Fig. 1d and e. The TEM images of HPFe-N-C exhibit mesoporous structures, particularly, without observed nanoparticles and nanoclusters. As revealed in Fig. 1e, the HRTEM image confirms the presence of edge and defect sites in HPFe-N-C, which will be beneficial for improving catalytic activity. The
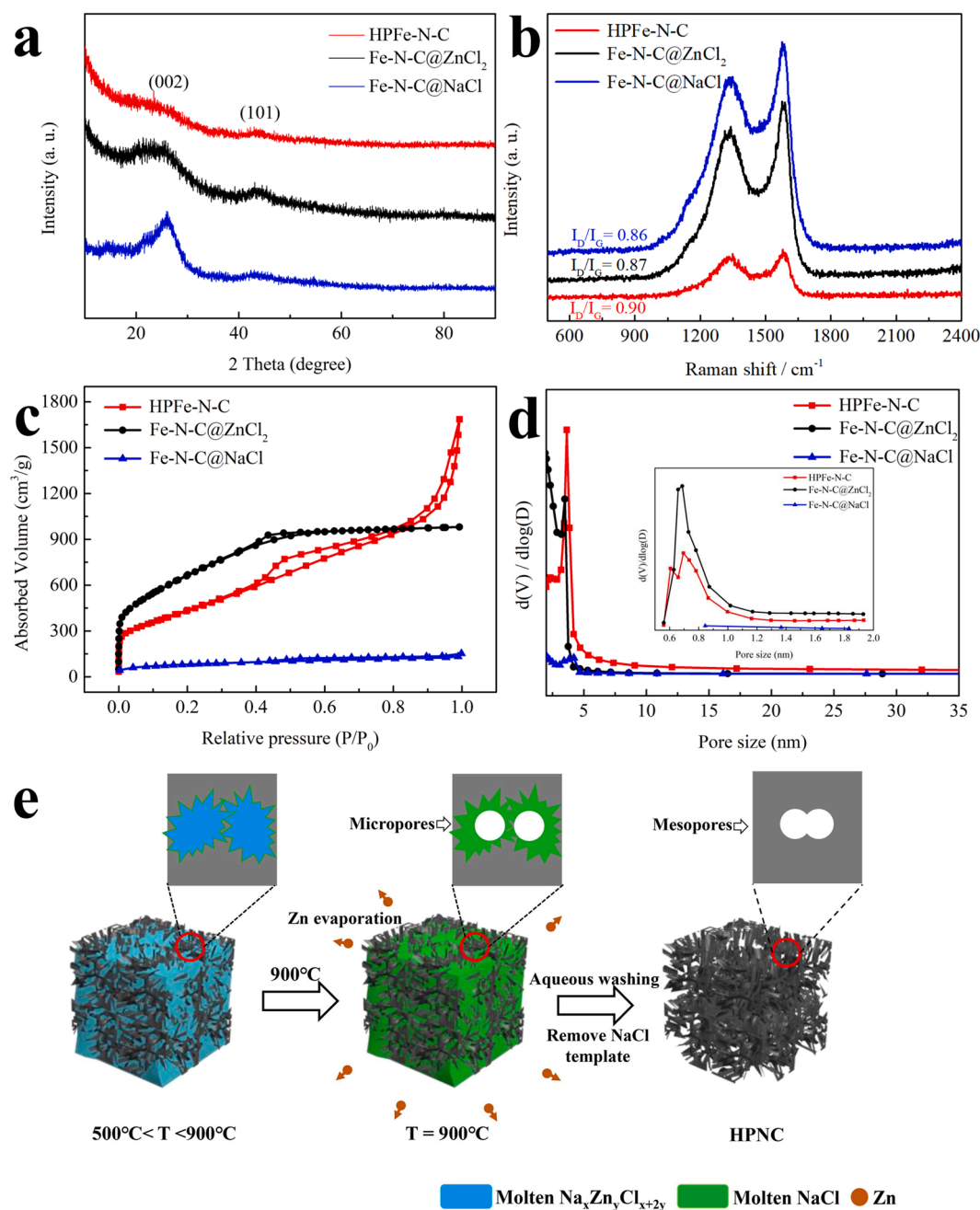
Fig. 2. (a) XRD spectra and (b) Raman spectra of the synthesized materials. (c) N_2 adsorption-desorption isotherms of the synthesized materials. (d) The pore size distribution of the synthesized materials. (e) Schematic illustration of the pore-forming mechanism of NaCl template.

dense white spots, assigned to abundant micropores, could be easily observed. In addition, the lattice fringe of about 0.34 nm is observed, corresponding to the (002) facet of graphite [37]. The selected area electron diffraction (SAED) image also suggests that no iron-based nanoparticles are generated in HPFe-N-C during pyrolysis. The spherical aberration corrected TEM was employed to directly observe atomically dispersed iron atoms. As shown in Fig. 1f, abundant isolated bright spots were observed, assigning to Fe-Nx sites. As shown in Fig. S2, the elemental mappings are conducted for HPFe-N-C, where iron and nitrogen are well distributed on hierarchically porous carbon. Based on the above results, atomically dispersed Fe-N_x sites are believed existing in the HPFe-N-C.

To further investigate the dual melt-salt-mediated templates derived Fe-N-C materials, the powder XRD is conducted. The synthesized materials present characteristic peaks of C(002) and (101) facets at about

$24°$ and $44°$ (Fig. 2a), which correspond to the typical carbon structure [4,38]. No diffraction peak associated with iron or iron carbides/oxides is observed in the XRD pattern of HPFe-N-C, suggesting no highly crystalline iron or iron carbides/oxides in the HPFe-N-C catalyst. Moreover, the defect level of prepared materials is analyzed by Raman spectroscopy. The synthesized samples exhibit typical peaks of defective sp3 carbon and graphitic sp2 carbon at about 1350 cm^{-1} (D-band) and 1590 cm^{-1} (G-band), respectively [39,40] (Fig. 2b). The I_D/I_G values of two reference samples employing single molten-salt are lower than that of HPFe-N-C (0.90), proving that more defect is generated for HPFe-N-C materials on account of the synergistic effect of $ZnCl_2$ and NaCl templates. The abundant defect structure is thought to promote the catalytic process [41].

To further analyze the synergistic effect of molten salt templates for hierarchical porous structure, especially the pore-forming mechanism of
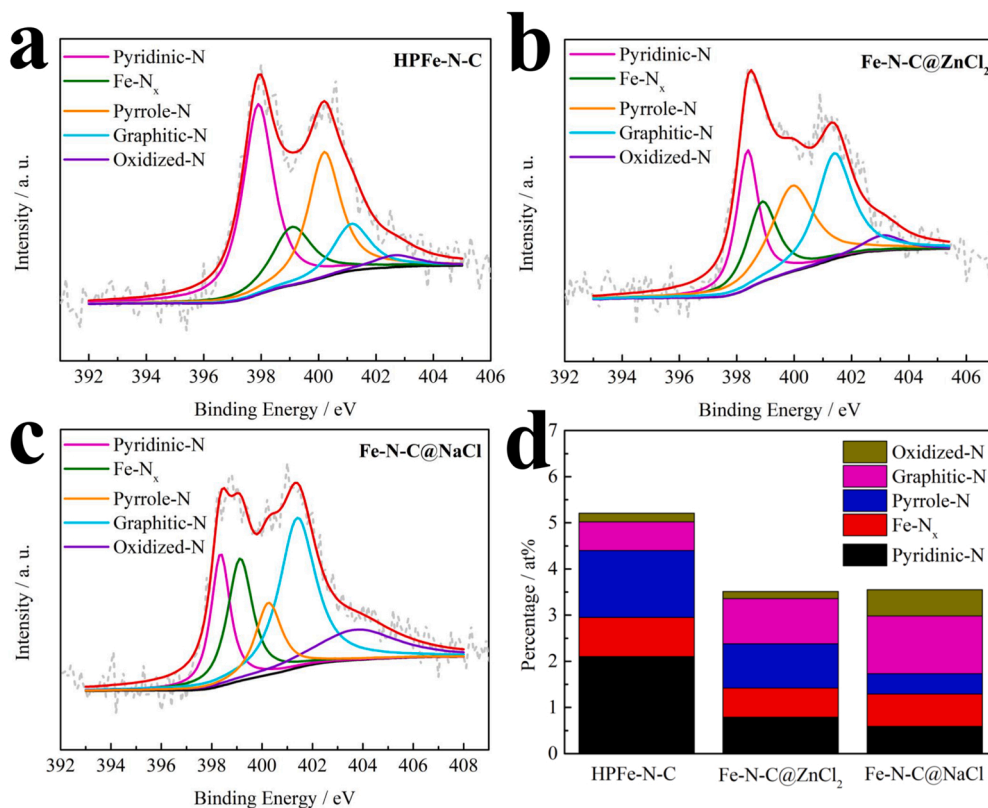
Fig. 3. (a–c) High-resolution N 1s spectra of the synthesized materials. (d) The corresponding concentration of various N species in the prepared materials.
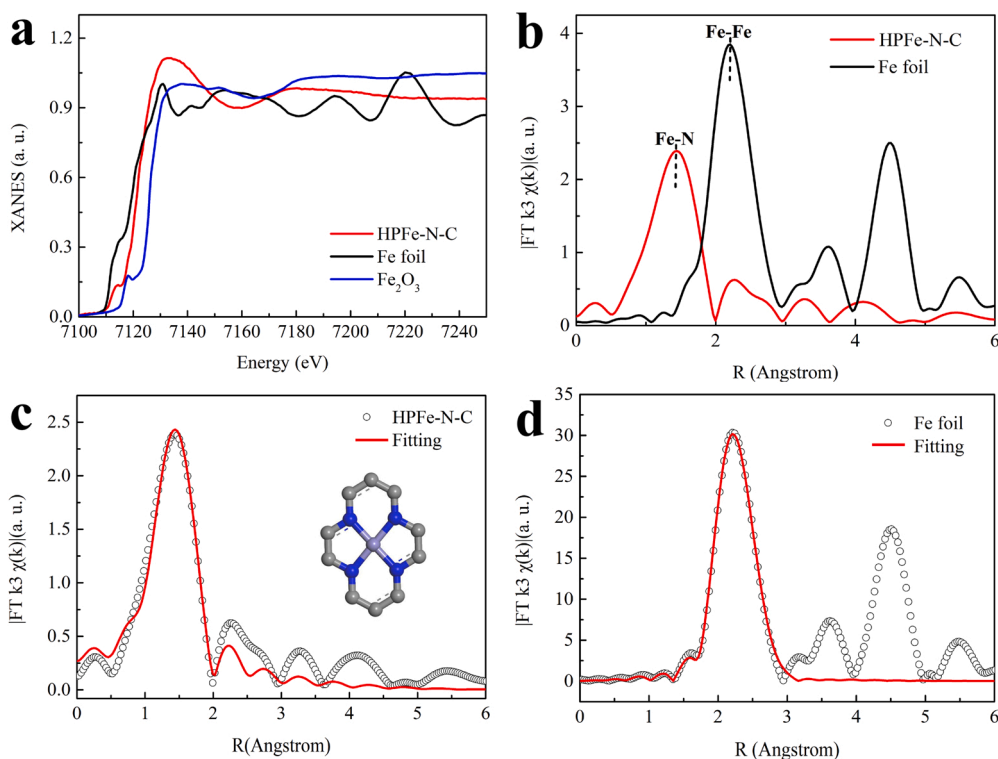

Fig. 4. (a) Fe K-edge XANES spectra. (b) FT-EXAFS curves. (c, d) FT-EXAFS fitting curve of HPFe-N-C and Fe foil.

NaCl template, N_2 adsorption/desorption methods are employed to evaluate the synthesized HPFe-N-C, Fe-N-C@ZnCl$_2$, Fe-N-C@NaCl materials and adenine precursor.

The isotherm of HPFe-N-C shows a remarkable uptake at low P/P_0 and a distinct type-IV hysteresis loop (Fig. 2c), suggesting the existence of micropores and mesopores, respectively [21,23,42]. In contrast, the
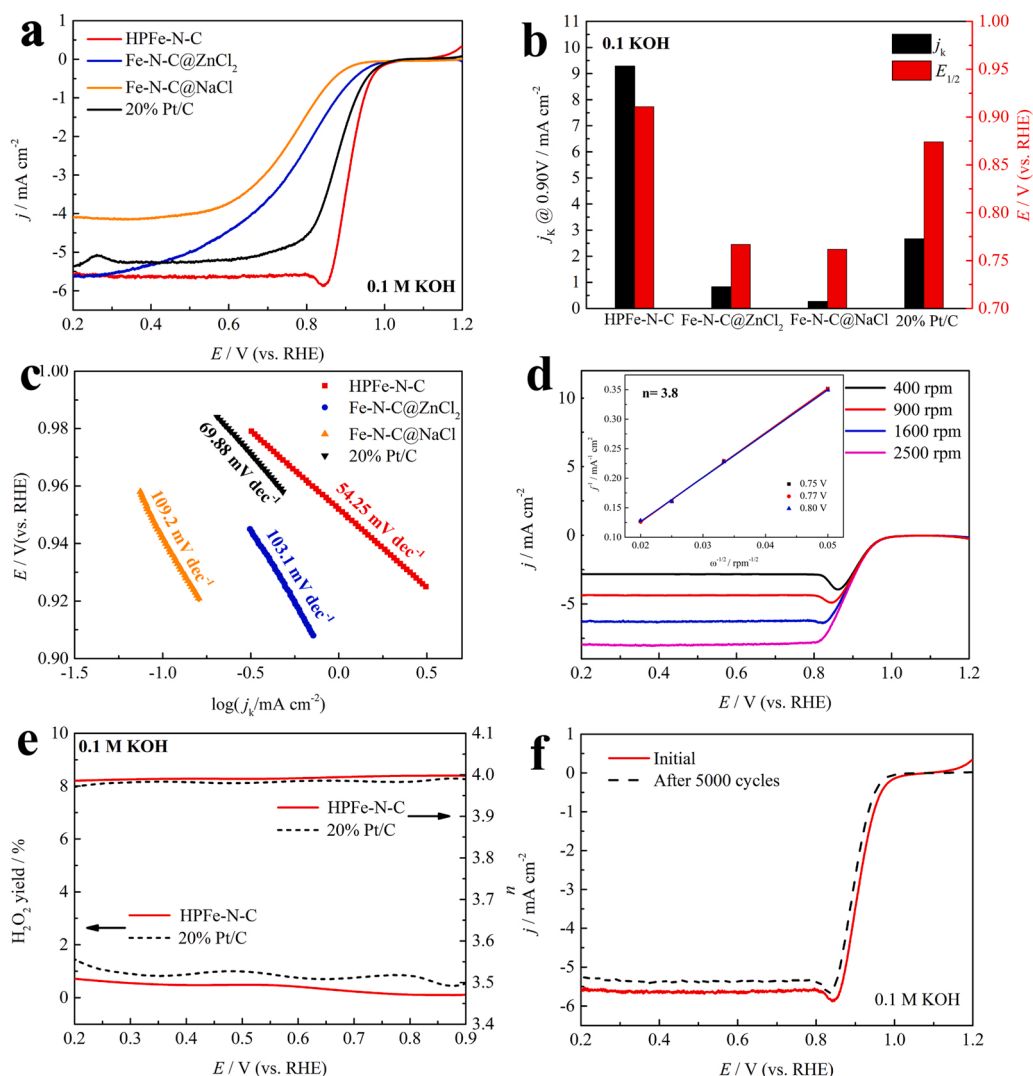
Fig. 5. (a) LSV curves of the synthesized materials and platinum/carbon in 0.1 M KOH. (b) j_K at 0.90 V and the half-wave potential. (c) Tafel plots of the synthesized materials and platinum/carbon. (d) LSV curves of HPFe-N-C at different rotational speeds and the K–L plots. (e) H_2O_2 yield and n. (f) The difference of HPFe-N-C before and after the stability test.

porous structure of Fe-N-C@NaCl is hard to observe, suggesting that the contribution of pure NaCl templates to the construction of porous structures is almost negligible. The Fe-N-C@ZnCl$_2$ presents a type-I isotherm, confirming that the pore framework of Fe-N-C@ZnCl$_2$ is primarily micropores, the mesopores structure are still lacking. Therefore, the synergistic effect of ZnCl$_2$ and NaCl is proved to be the key to the formation of hierarchically porous framework. The evaporation of the single ZnCl$_2$ template at 900 °C can obtain a large number of micropores. Particularly, the single NaCl template cannot directly construct porous structures, which is different from those previously reported works.

The pore structure analysis in Table S4 strongly support our viewpoint. In the micropores range of below 2 nm, the HPFe-N-C material presents lower S_{BET} (109.86 m^2 g^{-1}) and pore volume (V_{pore}) (0.0545 cm^3 g^{-1}) than the Fe-N-C@ZnCl$_2$ (421.14 m^2 g^{-1}; 0.2059 cm^3 g^{-1}). However, in the mesopore range of over 2 nm, the HPFe-N-C shows larger S_{BET} and greater V_{pore} than those of Fe-N-C@ZnCl$_2$. The results indicate the destruction of micropores walls and the merging of micropores into mesopores in HPFe-N-C, which can be further confirmed by the fact that HPFe-N-C material presents lower total BET area (1605.5620 vs. 2437.5568 m^2 g^{-1}) but higher total V_{pore} (2.8572 vs. 1.4761 cm^3 g^{-1}) than the Fe-N-C@ZnCl$_2$ material. Compared with

HPFe-N-C, the total surface area (275.8223 m^2 g^{-1}) and total V_{pore} (0.2026 cm^3 g^{-1}) of Fe-N-C@NaCl are negligible. Therefore, it is believed that NaCl cannot directly construct mesopores, but promotes the transformation of partial micropores (generated by the evaporation of Zn) into mesopores. As shown in Table S4, the adenine precursor has inappreciable S_{BET} (2.1952 m^2 g^{-1}) and V_{pore} (0.0181 cm^3 g^{-1}), further proving the critical role of dual melt-salt templates for the hierarchically porous structure. Abundant mesopores are conducive to efficient mass transfer and accessibility of active centers (Fig. S15), therefore, the HPFe-N-C material may present nice preference in Zn-air batteries.

The adenine in this work has a lower decomposition temperature (360 °C), compared with the common precursors in other works [35]. The low decomposition temperature results in the severe collapse of pore framework during the pyrolysis if using adenine. In principle, the molten salt as a template can prevent the direct decomposition of adenine, forming porous structures. However, in practice, the melting point temperature of NaCl is too high (801 °C) to protect adenine at temperature range between 360 and 801 °C. Therefore, the pore structure of Fe-N-C@NaCl in this work using adenine as precursor is reasonably inferior. On the other hand, ZnCl$_2$ as another important template has low melting point temperature of 283 °C, which is close to the decomposition temperature of adenine (360 °C). Therefore, the
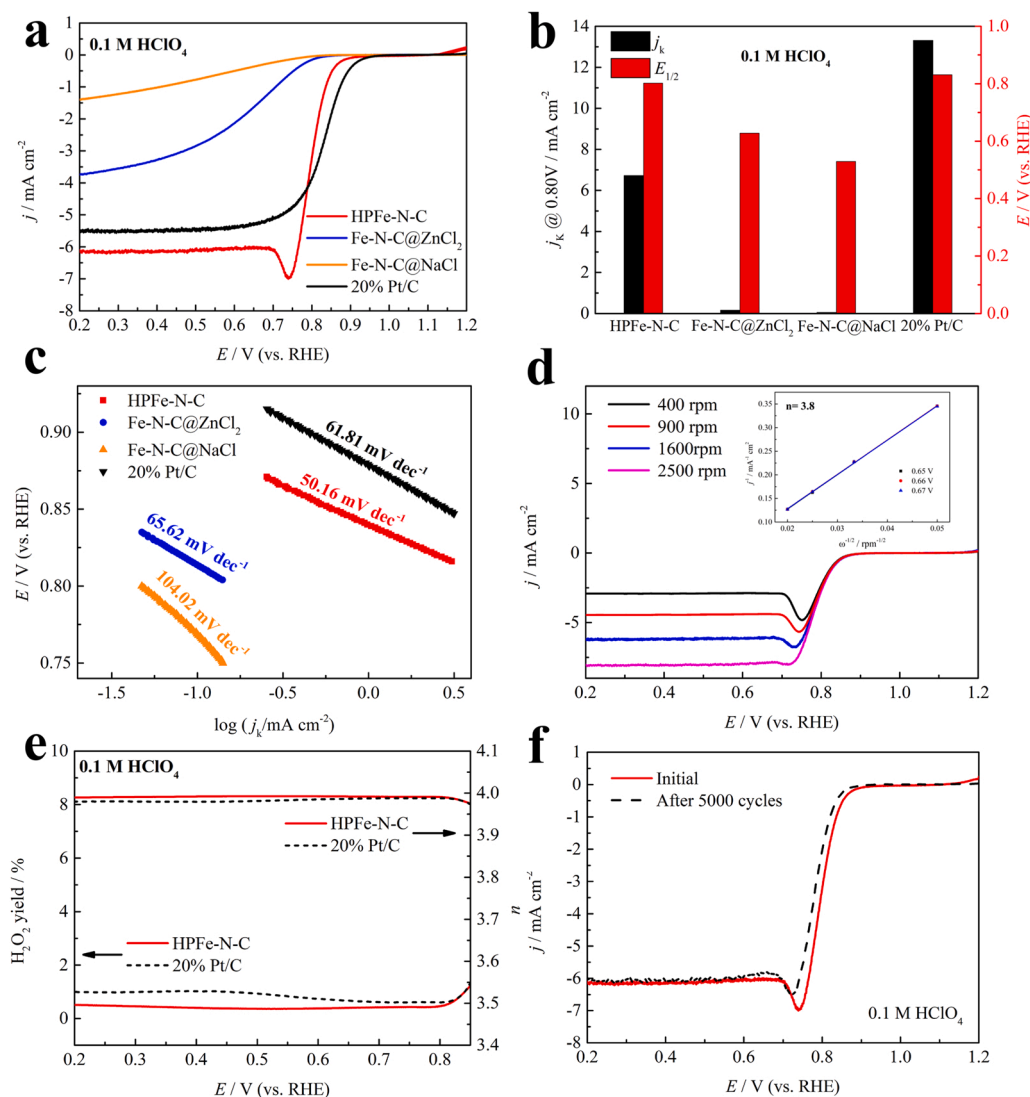
Fig. 6. (a) LSV curves of the synthesized materials and platinum/carbon in 0.1 M HClO₄. (b) j_K at 0.80 V and the half-wave potential. (c) Tafel plots of the synthesized materials and platinum/carbon. (d) LSV curves of HPFe-N-C at different rotational speeds and the K–L plots. (e) H₂O₂ yield and *n*. (f) The difference of HPFe-N-C before and after the stability test.

single ZnCl₂ template can afford the molten salt-confined space for whole pyrolysis process and form abundant pore structure. Even though, it has been well known that the evaporation of Zn usually results in micropores formation, so that the meso- and macro-pores are still lacking in the prepared materials. As a result, the Fe-N-C@ZnCl₂ using single ZnCl₂ template exhibits a low pore volume in this work. For the HPFe-N-C material, the synergistic effect of ZnCl₂ and NaCl templates plays a key role in the construction of hierarchical porous structures. According to the phase diagram (Fig. S16) of NaCl/ZnCl₂ (NaCl: 69 mol % in this work), the solid NaCl and solid Na₂ZnCl₄ coexist at low temperature (< 400 °C). As the temperature continues to rise, molten salt begins to appear (about 400 °C, close to the decomposition temperature of adenine), which provides protection for the adenine. At the same time, there are still some solid NaCl in the reaction system. When the temperature rises above 500 °C, the adenine is confined by the Na$_x$Zn$_y$Cl$_{x+2y}$ molten salt mixture. As shown in Fig. 2e, Zn evaporates at 900 °C, resulting in the formation of a large number of micropores, so that the residual molten salt is completely NaCl. The NaCl melt salt nanodroplet can promote the transformation of partial micropores (generated by the evaporation of Zn) into mesopores through the destruction and merging of micropores.

The elemental distribution and concentration of the synthesized materials are measured by XPS. The survey spectra confirm the characteristic peaks of Fe, N, O and C in these materials (see Fig. S3). The matching element contents are presented in the Table S1. The total N concentration of HPFe-N-C (5.21 at%) is higher than that of Fe-N-C@ZnCl₂ (3.51 at%) and Fe-N-C@NaCl (3.55 at%), suggesting that dual melt-salt templates can effectively reduce the loss of nitrogen during pyrolysis. As revealed in Fig. 3a–c, the high-resolution N 1s spectra for the prepared materials displays five peaks at 398.2 ± 0.3, 399 ± 0.3, 400 ± 0.3, 401.2 ± 0.3 eV and 402–404 eV, which can be ascribed to pyridinic N, Fe-N$_x$, pyrrole N, graphitic N and oxidized N species, respectively [43,44]. As revealed in Fig. 3d and Table S2, the concentration of active Fe-N$_x$ site [45,46] for HPFe-N-C (0.85 at%) is 1.35 times and 1.21 times higher than that of Fe-N-C@ZnCl₂ (0.63 at%) and Fe-N-C@NaCl (0.70 at%), respectively. The above results demonstrate that the synergistic effect of ZnCl₂ and NaCl templates could promote the formation of more Fe-N$_x$ sites. Therefore, the activity of HPFe-N-C for O₂ reduction may be better than Fe-N-C@ZnCl₂ and Fe-N-C@NaCl. In addition, pyridinic N is beneficial to boost the intrinsic catalytic performance, which can provide coordination sites for iron atoms and improve the adsorption capacity of O₂ [11,27]. Compared with Fe-N-C@ZnCl₂ (0.79 at%) and Fe-N-C@NaCl (0.59 at%), the HPFe-N-C exhibits a higher concentration of pyridinic N (2.10 at%). The
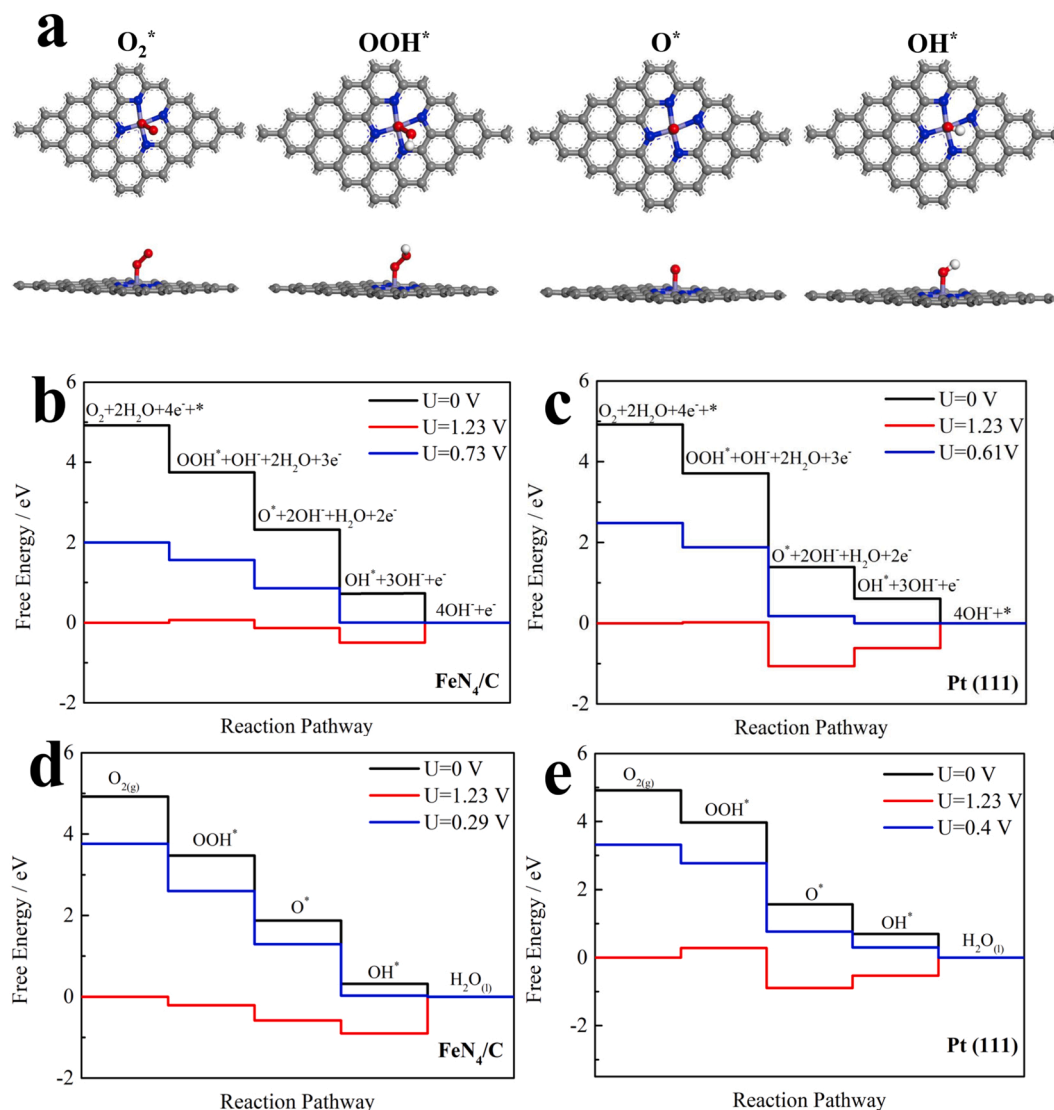
Fig. 7. (a) The stable models of intermediate species adsorbed on FeN_4/C. Free energy ladder diagrams of reaction pathway in (b and c) alkaline environment and (d and e) acidic environment.

high-resolution of Fe 2p spectra for all the catalysts show two pairs of peaks for Fe^{2+} and Fe^{3+} [9] (see in Fig. S4a-c). No signal belonging to zero-valence metallic iron is found in HPFe-N-C. This further suggests the atomically dispersed Fe-N_x features in HPFe-N-C material. The results of ICP-OES analysis reveal that Fe content in HPFe-N-C is 1.42 wt %.

According to the XANES spectra in Fig. 4a, the chemical valence state of iron in HPFe-N-C catalyst locates between the standard Fe foil and Fe_2O_3, i.e., between 0 and + 3. An obvious peak at 1.4 Å is observed for HPFe-N-C based on the EXAFS spectra (Fig. 4b), which indicates the well-defined Fe-N configuration. Importantly, no signal (2.2 Å) for Fe-Fe configuration can be found in the HPFe-N-C. These results, together with spherical aberration corrected TEM images, indicate that the isolated Fe-N_x sites are well distributed on the carbon substrates. Moreover, the EXAFS is fitted to estimate the coordination number of Fe-N_x sites. As presented in Fig. 4c and Table S5, the local Fe-N_x structure in HPFe-N-C is in good agreement with the theoretical Fe-N_4 model.

3.2. Electrochemical performance evaluation

The HPFe-N-C exhibits outstanding ORR activity under alkaline solution. Compare with the Fe-N-C@$ZnCl_2$ ($E_{1/2} = 0.767$ V) and Fe-N-C@NaCl ($E_{1/2} = 0.762$ V), the HPFe-N-C presents a much higher catalytic property with the $E_{1/2}$ of 0.911 V (Fig. 5a), indicating that the dual melt-salt-mediated template method is pivotal to improve the catalytic nature. Remarkably, the performance of HPFe-N-C is much higher than platinum/carbon ($E_{1/2} = 0.874$ V) under alkaline electrolyte. The prominent catalytic nature of HPFe-N-C is comparable to or even outperforms typical non-platinum materials in literature (Table S6). On the basis of the Koutechy-Levich (K-L) formula, HPFe-N-C exhibits a better kinetic current density (j_k) of 9.286 mA/cm^2 at 0.900 V (Fig. 5b), 3.48 times as that of platinum/carbon (2.666 mA/cm^2). In addition, the HPFe-N-C reveals a lower Tafel slope of 54.25 mV dec^{-1} than platinum/carbon (69.88 mV dec^{-1}), which further affirms its nice reaction kinetic (Fig. 5c). To further investigate the reaction pathway of HPFe-N-C under alkaline electrolyte, the LSV curves with diverse speeds are exhibited in Fig. 5d. The K-L plots of HPFe-N-C present excellent linearity. The electron transfer number (n) of HPFe-N-C is obtained as 3.8, suggesting a near $4e^-$ ORR process under alkaline electrolyte. RRDE tests are also used to evaluate the n and monitor the evolution of H_2O_2 yield under alkaline electrolyte. As exhibited in Fig. 5e, the HPFe-N-C material follows a near 4e- reaction pathway, which coincides with K-L plots. The yield of H_2O_2 for HPFe-N-C is consistently below 1%. The above results suggest the HPFe-N-C as a superior ORR catalyst. The stability is a necessary
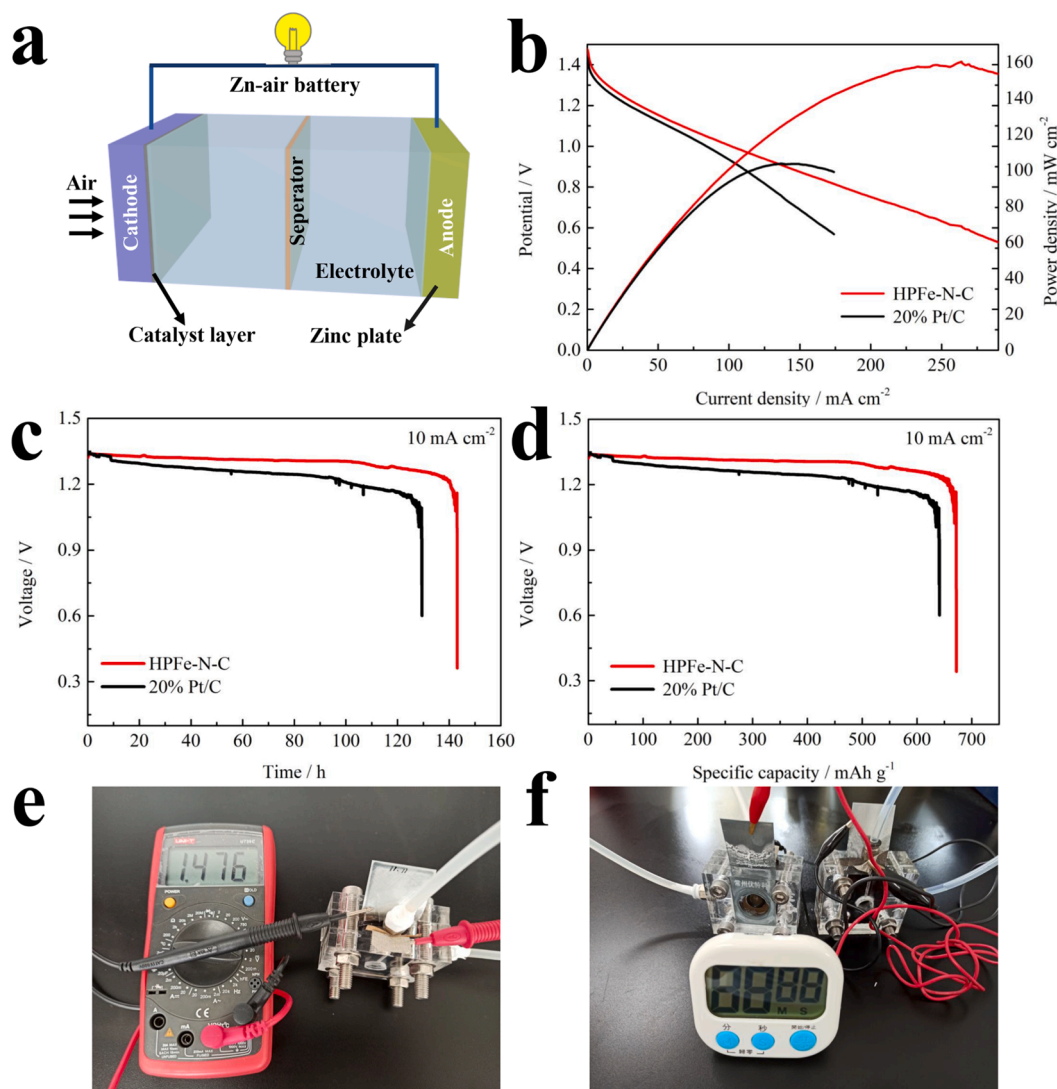
Fig. 8. (a) Structure model of a liquid ZAB. (b) Potential-current density curves and power density of liquid ZAB. (c) Discharging performance of liquid ZAB. (d) Specific capacities of liquid ZABs. (e) Photograph of the liquid ZAB measured by the voltmeter. (f) The digital photograph of the electronic clock powered by a couple of liquid ZABs using HPFe-N-C as the ORR catalysts.

criterion for catalysts in the practical applications. In this work, ADT methods are employed to measure the durability of HPFe-N-C. A negligible decay in $E_{1/2}$ (only 10 mV) for HPFe-N-C can be observed after 5000 CV cycles in 0.1 M KOH (Fig. 5f). In contrast, there is a dramatic decay in $E_{1/2}$ for platinum/carbon (36 mV) (Fig. S5a), indicating that HPFe-N-C presents more outstanding durability than platinum/carbon in potassium hydroxide solution.

Moreover, Among the three tested samples, the HPFe-N-C exhibits the highest double layer capacitance (C_{dl}) of 85.93 mF cm^{-2} (Fig. S6d). Because the electrochemical surface area (ECSA) increases with the increasing of C_{dl}, the HPFe-N-C material is considered to have the largest ECSA.

The HPFe-N-C catalyst presents nice oxygen reduction activity under acidic electrolyte. The LSV curves demonstrate that the half-wave potential of HPFe-N-C in 0.1 M HClO$_4$ is 0.802 V (Fig. 6a), not quite far from that of platinum/carbon (0.831 V), which is far greater than that of other control samples. The prominent catalytic property of HPFe-N-C is comparable to or even outperforms typical Fe-N-C materials in various papers (Table S7). In addition, as presented in Fig. 6b, the j_K of HPFe-N-C at 0.800 V is 6.713 mA/cm^2, not quite far from the Pt/C (13.304 mA/cm^2). Further, the better reaction kinetics of HPFe-N-C is revealed with a lower Tafel slope (50.16 mV dec^{-1}) (Fig. 6c). According the K-L

formula, the n of HPFe-N-C in 0.1 M HClO$_4$ is about 3.8 (Fig. 6d), suggesting a 4e$^-$ ORR pathway in acidic solution. As presented in Fig. 6e, the n is evaluated by RRDE as 3.97 ~ 3.99, and it has a low H$_2$O$_2$ yield ($< 2\%$), indicating that the HPFe-N-C material favors a 4e$^-$ reaction pathway under acidic solution. On the other hand, as exhibited from Fig. 6f, the HPFe-N-C shows nice electrochemical durability with a not obvious decline in half-wave potential (16 mV) after the ADT test in 0.1 M HClO$_4$, which is almost same as platinum/carbon (17 mV) (Fig. S5b).

We emphasize that the dual melt-salt-mediated template strategy in this work is universal as different metal-Phen complexes have been applied (metal = Co and Mn) to synthesize various 3D porous MN$_x$/C materials for cathode. As shown in Fig. S8, both HPCo-N-C and HPMn-N-C catalysts display satisfactory O$_2$ reduction activity in potassium hydroxide solution, demonstrating the dual melt-salt-mediated template strategy is appropriate to different M-N-C materials.

3.3. Catalytic mechanisms revealed by DFT calculations

To better reveal the advances of HPFe-N-C as an ORR catalyst, DFT methods are utilized to study the energy variation of each steps on the catalyst models [47]. Based on the results of EXAFS fitting analysis,
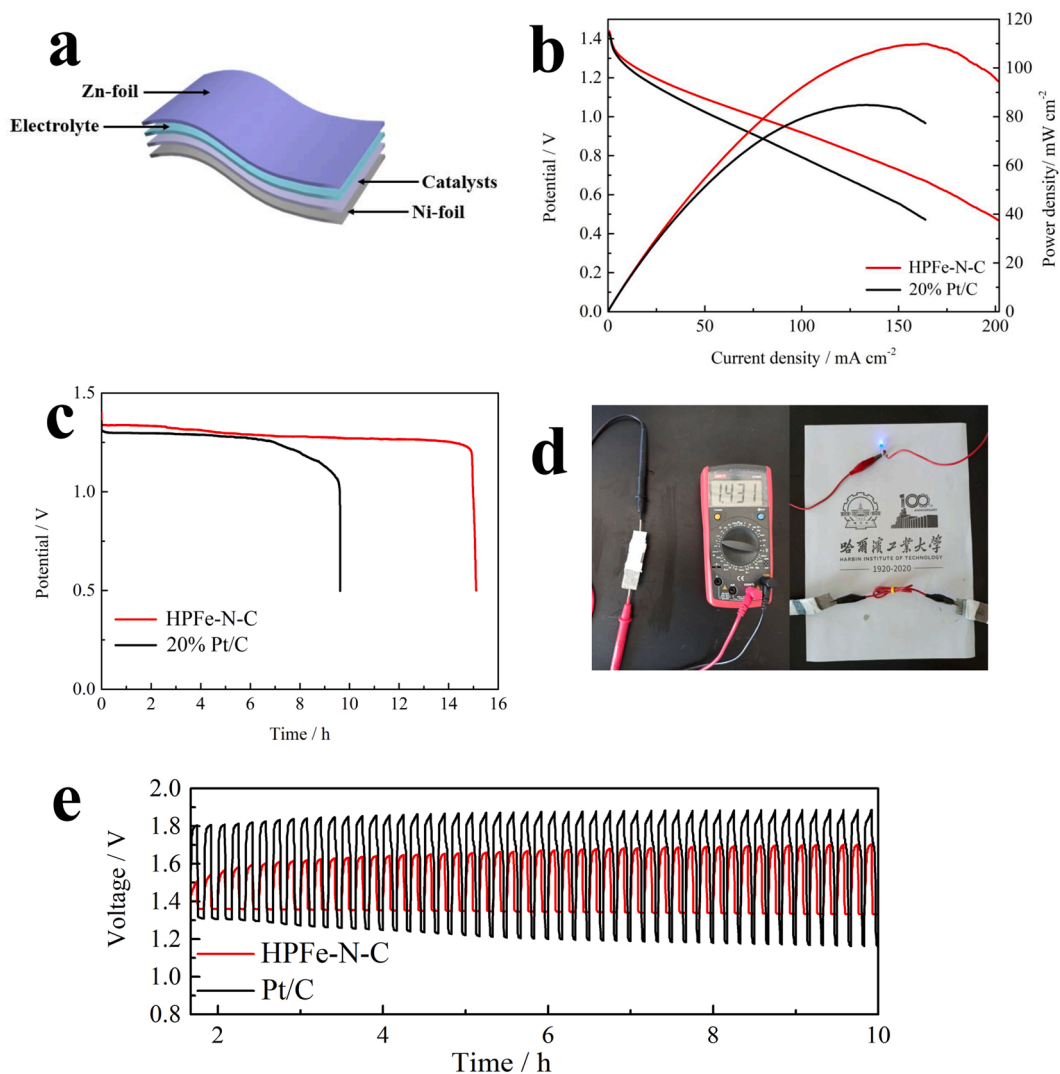
Fig. 9. (a) Structure model of a solid ZAB. (b) Potential-current density curves and corresponding power density. (c) Discharge test of the solid ZAB (2 mA/cm²). (d) Photographs of the OCV and a colourful light emitting diode lightened by solid ZABs. (e) Cycling property of the solid ZAB.

Fe-N$_4$ is considered to be the most dominant active site of HPFe-N-C [48–50]. Therefore, the FeN$_4$ embedded in a carbon layer and Pt (111) plane as the active site for HPFe-N-C and 20% platinum/carbon are modeled (Fig. 7a, Fig. S10-S11), respectively [22]. At U = 0 V in the alkaline solution (Fig. 7b-c), all steps on FeN$_4$ and Pt (111) surface show downhill process, indicating the oxygen reduction can proceed smoothly on the catalysts surface under this condition. For Fe-N$_4$, the OH* desorption step exhibits the most significant variation in free energy. Thus, the OH* desorption is the rate-determining step over FeN$_4$ and the corresponding limiting barrier is − 0.73 eV. In contrast, the limiting barrier over the Pt (111) is − 0.61 eV. Therefore, the FeN$_4$ site of HPFe-N-C is more beneficial to oxygen reduction than the Pt (111) plane of Pt/C in the alkaline environments, consistently with the result of electrochemical test. At U = 1.23 V, two elementary reactions on Fe-N$_4$ and three elementary reactions on Pt (111) are thermodynamically unfavorable. Only when potential drops to 0.73 V, the entire elementary reactions on Fe-N$_4$ become downhill, therefore, the thermodynamic limiting potential (U$_L$) of Fe-N$_4$ is 0.73 V under alkaline solution; in contrast, the Pt (111) presents a lower U$_L$ of 0.61 V, demonstrating that the HPFe-N-C presents a better intrinsic activity than platinum/carbon under alkaline environment. Moreover, the rate-determining step on the FeN$_4$ and Pt (111) in the acidic solution is the transformation from OH* into H$_2$O (see in Fig. 7d and e). However, the ORR process over Fe-N$_4$

site shows a more positive value of limiting barrier (− 0.32 eV) and a lower thermodynamic limiting potential (0.29 eV) than those of Pt (111) (− 0.69 eV; 0.4 eV), suggesting the activity of HPFe-N-C is still not ideal in acidic environment.

3.4. Zn-air battery performance evaluation

On account of the nice oxygen reduction performance of HPFe-N-C, it is further applied in the oxygen cathode in the liquid ZABs. The open-circuit voltage (OCV) of liquid ZABs using HPFe-N-C (1.477 V) exceeds that of liquid ZABs using platinum/carbon (1.433 V) (Fig. 8b). The liquid ZAB using HPFe-N-C presents a peak power density of 160 mW cm^{-2}, which surpasses the platinum/carbon ZAB (103 mW cm^{-2}) and most non-platinum ZABs exhibited in previous articles (see in Table S8). Moreover, the long-term lifetime of the HPFe-N-C-based liquid ZAB is proved by the continuous discharge test at 10 mA/cm^2. The liquid ZAB employing HPFe-N-C shows a low voltage loss of 49.8 mV after 120-h operation (Fig. 8c). However, the Pt/C based liquid ZAB shows a large voltage loss of 177.32 mV after the same discharge test. In addition, the stability of HPFe-N-C based liquid ZABs at various current densities is also demonstrated (Fig. S13). The specific capacity and energy density of HPFe-N-C based battery (672 mA h g$_{Zn}^{-1}$; 853 Wh kg^{-1}) are higher than those of platinum/

carbon-based battery (641 mA h g_{Zn}^{-1}; 787 Wh kg^{-1}) (Fig. 8d, Fig. S14). The photograph in Fig. 8e presents an OCV of 1.476 V for HPFe-N-C based liquid ZAB. A group of liquid ZABs connected together are able to power up an electric clock (Fig. 8f). These consequences confirm that HPFe-N-C is a promising ORR catalyst.

The flexible electronic devices will be the research hotspot in the future, so that it is interesting to develop the flexible solid ZABs [11]. Fig. 9a reveals the structure model of a solid ZAB in this work. As shown in Fig. 9b, the solid ZAB using HPFe-N-C material (109 mW cm^{-2}) presents a better peak power density than platinum/carbon (84 mW cm^{-2}). Moreover, Fig. 9c exhibits a stable discharge voltage for 14 h at 2 mA/cm^2 in a solid ZAB using HPFe-N-C, suggesting a long-term durability. As shown in Fig. 9d, a photograph of a solid ZAB employing HPFe-N-C presents an OCV of 1.431 V measured by a voltmeter, and a couple of solid batteries can light the blue lamp, confirming the solid battery using HPFe-N-C material have practicability. The solid battery using HPFe-N-C also possess a certain charge/discharge property (Fig. 9e).

4. Conclusions

In a word, our work develops the dual melt-salt-mediated templating strategy to tailor the 3D hierarchically porous Fe-N-C material incorporated with abundant and highly accessible Fe-N$_4$ site. The ZnCl$_2$ and NaCl templates are used to construct the micropores and mesopores, respectively. The encapsulation of dual melt-salt templates, like a protector, effectively avoids the loss of N-containing active species. The hierarchically micro-mesopores structure with large specific surface area not only remits the agglomeration during pyrolysis, but also promotes the mass transport and the exposure of active Fe-N$_4$ site. Benefiting from the synergistic effect of high-density Fe-N$_4$ site, unique porous structure and high defect degree, the optimized HPFe-N-C reveals satisfactory catalytic performance and electrochemical stability in alkaline and acidic electrolyte. Further, the liquid ZAB and solid ZAB employing HPFe-N-C as the catalysts achieve better peak power density as well as discharge durability than those using platinum/carbon. The DFT calculations prove that the FeN$_4$ site with high thermodynamic limiting potential is the dominating ORR active center in the HPFe-N-C; while the transformation processes OH* → OH$^-$ and OH* → H$_2$O are the rate determining step over the HPFe-N-C under alkaline and acidic electrolyte, respectively. Our research affords the universal strategy to tailor porous structure in M-N-C catalysts.

CRediT authorship contribution statement

Hao Xu: Data curation, Writing – original draft. **Dan Wang:** Formal analysis. **Peixia Yang:** Conceptualization, Writing – review & editing. **Lei Du:** Conceptualization, Writing – review & editing. **Xiangyu Lu:** Investigation, Software. **Ruopeng Li:** Investigation, Software. **Lilai Liu:** Investigation, Software. **Jinqiu Zhang:** Writing – review & editing. **Maozhong An:** Writing – review & editing.

Declaration of Competing Interest

The authors declare that they have no known competing financial interests or personal relationships that could have appeared to influence the work reported in this paper.

Acknowledgements

Appendix A. Supporting information

Supplementary data associated with this article can be found in the online version at doi:10.1016/j.apcatb.2021.121040.

References

[1] Y. Chang, J. Chen, J. Jia, X. Hu, H. Yang, M. Jia, Z. Wen, The fluorine-doped and defects engineered carbon nanosheets as advanced electrocatalysts for oxygen electroreduction, Appl. Catal. B: Environ. 284 (2021), 119721, https://doi.org/10.1016/j.apcatb.2020.119721.

[2] X. Fu, G. Jiang, G. Wen, R. Gao, S. Li, M. Li, J. Zhu, Y. Zheng, Z. Li, Y. Hu, L. Yang, Z. Bai, A. Yu, Z. Chen, Densely accessible Fe-Nx active sites decorated mesoporous-carbon-spheres for oxygen reduction towards high performance aluminum-air flow batteries, Appl. Catal. B: Environ. 293 (2021), 120176, https://doi.org/10.1016/j.apcatb.2021.120176.

[3] C. Lai, J. Fang, X. Liu, M. Gong, T. Zhao, T. Shen, K. Wang, K. Jiang, D. Wang, In situ coupling of NiFe nanoparticles with N-doped carbon nanofibers for Zn-air batteries driven water splitting, Appl. Catal. B: Environ. 285 (2021), 119856, https://doi.org/10.1016/j.apcatb.2020.119856.

[4] M. Mazzucato, G. Daniel, A. Mehmood, T. Kosmala, G. Granozzi, A. Kucernak, C. Durante, Effects of the induced micro- and meso-porosity on the single site density and turn over frequency of Fe-N-C carbon electrodes for the oxygen reduction reaction, Appl. Catal. B: Environ. 291 (2021), 120068, https://doi.org/10.1016/j.apcatb.2021.120068.

[5] X. Qu, Y. Han, Y. Chen, J. Lin, G. Li, J. Yang, Y. Jiang, S. Sun, Stepwise pyrolysis treatment as an efficient strategy to enhance the stability performance of Fe-N$_X$/C electrocatalyst towards oxygen reduction reaction and proton exchange membrane fuel cell, Appl. Catal. B: Environ. 295 (2021), 120311, https://doi.org/10.1016/j.apcatb.2021.120311.

[6] A. Wang, C. Zhao, M. Yu, W. Wang, Trifunctional Co nanoparticle confined in defect-rich nitrogen-doped graphene for rechargeable Zn-air battery with a long lifetime, Appl. Catal. B: Environ. 281 (2021), 119514, https://doi.org/10.1016/j.apcatb.2020.119514.

[7] Y. Wang, N. Xu, R. He, L. Peng, D. Cai, J. Qiao, Large-scale defect-engineering tailored tri-doped graphene as a metal-free bifunctional catalyst for superior electrocatalytic oxygen reaction in rechargeable Zn-air battery, Appl. Catal. B: Environ. 285 (2021), 119811, https://doi.org/10.1016/j.apcatb.2020.119811.

[8] Q. Zhou, S. Hou, Y. Cheng, R. Sun, W. Shen, R. Tian, J. Yang, H. Pang, L. Xu, K. Huang, Y. Tang, Interfacial engineering Co and MnO within N, S co-doped carbon hierarchical branched superstructures toward high-efficiency electrocatalytic oxygen reduction for robust Zn-air batteries, Appl. Catal. B: Environ. 295 (2021), 120281, https://doi.org/10.1016/j.apcatb.2021.120281.

[9] Y. Chen, Z. Li, Y. Zhu, D. Sun, X. Liu, L. Xu, Y. Tang, Atomic Fe dispersed on N-doped carbon hollow nanospheres for high-efficiency electrocatalytic oxygen reduction, Adv. Mater. 31 (2019), 1806312, https://doi.org/10.1002/adma.201806312.

[10] X. Yu, S. Lai, S. Xin, S. Chen, X. Zhang, X. She, T. Zhan, X. Zhao, D. Yang, Coupling of iron phthalocyanine at carbon defect site via π-π stacking for enhanced oxygen reduction reaction, Appl. Catal. B: Environ. 280 (2021), 119437, https://doi.org/10.1016/j.apcatb.2020.119437.

[11] H. Jin, H. Zhou, D. He, Z. Wang, Q. Wu, Q. Liang, S. Liu, S. Mu, MOF-derived 3D Fe-N-S co-doped carbon matrix/nanotube nanocomposites with advanced oxygen reduction activity and stability in both acidic and alkaline media, Appl. Catal. B Environ. 250 (2019) 143–149, https://doi.org/10.1016/j.apcatb.2019.03.013.

[12] M.G. Hao, R.M. Dun, Y.M. Su, W.M. Li, Highly active Fe-N-doped porous hollow carbon nanospheres as oxygen reduction electrocatalysts in both acidic and alkaline media, Nanoscale 12 (2020) 15115–15127, https://doi.org/10.1039/d0nr02763d.

[13] L. Cao, Y. Ma, A. Song, L. Bai, P. Zhang, X. Li, G. Shao, Stable composite of flower-like NiFe-layered double hydroxide nucleated on graphene oxide as an effective catalyst for oxygen reduction reaction, Int. J. Hydrogen Energy 44 (2019) 5912–5920, https://doi.org/10.1016/j.ijhydene.2019.01.075.

[14] F. Xiao, G.-L. Xu, C.-J. Sun, M. Xu, W. Wen, Q. Wang, M. Gu, S. Zhu, Y. Li, Z. Wei, X. Pan, J. Wang, K. Amine, M. Shao, Nitrogen-coordinated single iron atom catalysts derived from metal organic frameworks for oxygen reduction reaction, Nano Energy 61 (2019) 60–68, https://doi.org/10.1016/j.nanoen.2019.04.033.

[15] H. Zhang, H.T. Chung, D.A. Cullen, S. Wagner, U.I. Kramm, K.L. More, P. Zelenay, G. Wu, High-performance fuel cell cathodes exclusively containing atomically dispersed iron active sites, Energy Environ. Sci. 12 (2019) 2548–2558, https://doi.org/10.1039/c9ee00877b.

[16] Y. Cheng, S. He, S. Lu, J.P. Veder, B. Johannessen, L. Thomsen, M. Saunders, T. Becker, R. De Marco, Q. Li, S.Z. Yang, S.P. Jiang, Iron single atoms on graphene as nonprecious metal catalysts for high-temperature polymer electrolyte membrane fuel cells, Adv. Sci. 6 (2019), 1802066, https://doi.org/10.1002/advs.201802066.

[17] Y. Ma, A. Song, S. Yan, H. He, G. Shao, Direct solid-state growth of Fe/N Co-doped coordination structure between carbon nanotubes and ultra-thin porous carbon nanosheets towards oxygen reduction reaction, Electrochim. Acta 353 (2020), 136568, https://doi.org/10.1016/j.electacta.2020.136568.

[18] A. Song, L. Cao, W. Yang, W. Yang, L. Wang, Z. Ma, G. Shao, In situ construction of nitrogen-doped graphene with surface-grown carbon nanotubes as a multifactorial synergistic catalyst for oxygen reduction, Carbon 142 (2019) 40–50, https://doi.org/10.1016/j.carbon.2018.09.088.

[19] X.F. Lu, Y. Chen, S. Wang, S. Gao, X.W.D. Lou, Interfacing manganese oxide and cobalt in porous graphitic carbon polyhedrons boosts oxygen electrocatalysis for Zn-air batteries, Adv. Mater. 31 (2019), 1902339, https://doi.org/10.1002/adma.201902339.

[20] X.F. Lu, B.Y. Xia, S.Q. Zang, X.W.D. Lou, Metal-organic frameworks based electrocatalysts for the oxygen reduction reaction, Angew. Chem. Int. Ed. 59 (2020) 4634–4650, https://doi.org/10.1002/anie.201910309.

[21] L. Tong, Y.C. Wang, M.X. Chen, Z.Q. Chen, Q.Q. Yan, C.L. Yang, Z.Y. Zhou, S. Q. Chu, X. Feng, H.W. Liang, Hierarchically porous carbons as supports for fuel cell electrocatalysts with atomically dispersed Fe-Nx moieties, Chem. Sci. 10 (2019) 8236–8240, https://doi.org/10.1039/c9sc01154d.

[22] Z. Miao, X. Wang, M.-C. Tsai, Q. Jin, J. Liang, F. Ma, T. Wang, S. Zheng, B.-J. Hwang, Y. Huang, S. Guo, Q. Li, Atomically dispersed Fe-Nx/C electrocatalyst boosts oxygen catalysis via a new metal-organic polymer supramolecule strategy, Adv. Energy Mater. 8 (2018), 1801226, https://doi.org/10.1002/aenm.201801226.

[23] X.F. Lu, S.L. Zhang, E. Shangguan, P. Zhang, S. Gao, X.W.D. Lou, Nitrogen-doped cobalt pyrite yolk-shell hollow spheres for long-life rechargeable Zn-air batteries, Adv. Sci. 7 (2020) 2001178, https://doi.org/10.1002/advs.202001178.

[24] L. Wu, B. Ni, R. Chen, P. Sun, T. Chen, A general approach for hierarchically porous metal/N/C nanosphere electrocatalysts: nano-confined pyrolysis of in situ-formed amorphous metal–ligand complexes, J. Mater. Chem. A 8 (2020) 21026–21035, https://doi.org/10.1039/d0ta07029g.

[25] K. Yuan, D. Lutzenkirchen-Hecht, L. Li, L. Shuai, Y. Li, R. Cao, M. Qiu, X. Zhuang, M.K.H. Leung, Y. Chen, U. Scherf, Boosting oxygen reduction of single iron active sites via geometric and electronic engineering: Nitrogen and phosphorus dual coordination, J. Am. Chem. Soc. 142 (2020) 2404–2412, https://doi.org/10.1021/jacs.9b11852.

[26] H. Zhang, X.F. Lu, Z.P. Wu, X.W.D. Lou, Emerging multifunctional single-atom catalysts/nanozymes, ACS Cent. Sci. 6 (2020) 1288–1301, https://doi.org/10.1021/acscentsci.0c00512.

[27] D. Wang, H. Xu, P. Yang, L. Xiao, L. Du, X. Lu, R. Li, J. Zhang, M. An, A dual-template strategy to engineer hierarchically porous Fe–N–C electrocatalysts for the high-performance cathodes of Zn–air batteries, J. Mater. Chem. A 9 (2021) 9761–9770, https://doi.org/10.1039/d1ta00585e.

[28] C. Zhu, Q. Shi, B.Z. Xu, S. Fu, G. Wan, C. Yang, S. Yao, J. Song, H. Zhou, D. Du, S. P. Beckman, D. Su, Y. Lin, Hierarchically porous M-N-C (M = Co and Fe) single-atom electrocatalysts with robust MNx active moieties enable enhanced ORR performance, Adv. Energy Mater. 8 (2018), 1801956, https://doi.org/10.1002/aenm.201801956.

[29] G. Chen, P. Liu, Z. Liao, F. Sun, Y. He, H. Zhong, T. Zhang, E. Zschech, M. Chen, G. Wu, J. Zhang, X. Feng, Zinc-mediated template synthesis of Fe-N-C electrocatalysts with densely accessible Fe-Nx active sites for efficient oxygen reduction, Adv. Mater. 32 (2020), e1907399, https://doi.org/10.1002/adma.201907399.

[30] Z.X. Mao, M.J. Wang, L. Liu, L. Peng, S. Chen, L. Li, J. Li, Z. Wei, ZnCl$_2$ salt facilitated preparation of FeNC: Enhancing the content of active species and their exposure for highly-efficient oxygen reduction reaction, Chin. J. Catal. 41 (2020) 799–806, https://doi.org/10.1016/s1872-2067(19)63405-4.

[31] M. Wang, W. Yang, X. Li, Y. Xu, L. Zheng, C. Su, B. Liu, Atomically dispersed Fe–heteroatom (N, S) bridge sites anchored on carbon nanosheets for promoting oxygen reduction reaction, ACS Energy Lett. 6 (2021) 379–386, https://doi.org/10.1021/acsenergylett.0c02484.

[32] D. Wu, J. Hu, C. Zhu, J. Zhang, H. Jing, C. Hao, Y. Shi, Salt melt synthesis of Chlorella-derived nitrogen-doped porous carbon with atomically dispersed CoN$_4$ sites for efficient oxygen reduction reaction, J. Colloid Interfaces Sci. 586 (2021) 498–504, https://doi.org/10.1016/j.jcis.2020.10.115.

[33] Y. Zhang, L.-B. Huang, W.-J. Jiang, X. Zhang, Y.-Y. Chen, Z. Wei, L.-J. Wan, J.-S. Hu, Sodium chloride-assisted green synthesis of a 3D Fe–N–C hybrid as a highly active electrocatalyst for the oxygen reduction reaction, J. Mater. Chem. A 4 (2016) 7781–7787, https://doi.org/10.1039/c6ta01655c.

[34] R. Wu, X. Wan, J. Deng, X. Huang, S. Chen, W. Ding, L. Li, Q. Liao, Z. Wei, NaCl protected synthesis of 3D hierarchical metal-free porous nitrogen-doped carbon catalysts for the oxygen reduction reaction in acidic electrolyte, Chem. Commun. 55 (2019) 9023–9026, https://doi.org/10.1039/c9cc02986a.

[35] J. Hu, D. Wu, C. Zhu, C. Hao, C. Xin, J. Zhang, J. Guo, N. Li, G. Zhang, Y. Shi, Melt-salt-assisted direct transformation of solid oxide into atomically dispersed FeN$_4$ sites on nitrogen-doped porous carbon, Nano Energy 72 (2020), 104670, https://doi.org/10.1016/j.nanoen.2020.104670.

[36] J. Li, S. Chen, W. Li, R. Wu, S. Ibraheem, J. Li, W. Ding, L. Li, Z. Wei, A eutectic salt-assisted semi-closed pyrolysis route to fabricate high-density active-site hierarchically porous Fe/N/C catalysts for the oxygen reduction reaction, J. Mater. Chem. A 6 (2018) 15504–15509, https://doi.org/10.1039/c8ta05419c.

[37] X. Xiao, X. Li, Z. Wang, G. Yan, H. Guo, Q. Hu, L. Li, Y. Liu, J. Wang, Robust template-activator cooperated pyrolysis enabling hierarchically porous honeycombed defective carbon as highly-efficient metal-free bifunctional electrocatalyst for Zn-air batteries, Appl. Catal. B: Environ. 265 (2020), 118603, https://doi.org/10.1016/j.apcatb.2020.118603.

[38] X. Luo, X. Wei, H. Wang, W. Gu, T. Kaneko, Y. Yoshida, X. Zhao, C. Zhu, Secondary-atom-doping enables robust Fe–N–C single-atom catalysts with enhanced oxygen reduction reaction, Nano-Micro Lett. 12 (2020) 163, https://doi.org/10.1007/s40820-020-00502-5.

[39] Y. Deng, B. Chi, X. Tian, Z. Cui, E. Liu, Q. Jia, W. Fan, G. Wang, D. Dang, M. Li, K. Zang, J. Luo, Y. Hu, S. Liao, X. Sun, S. Mukerjee, g-C$_3$N$_4$ promoted MOF derived hollow carbon nanopolyhedra doped with high density/fraction of single Fe atoms as an ultra-high performance non-precious catalyst towards acidic ORR and PEM fuel cells, J. Mater. Chem. A 7 (2019) 5020–5030, https://doi.org/10.1039/c8ta11785c.

[40] Y. Yang, C. Wang, S. Gao, K. Mao, G. Xia, Z. Lin, P. Jiang, L. Hu, Q. Chen, Incorporation of Cu-Nx cofactors into graphene encapsulated Co as biomimetic electrocatalysts for efficient oxygen reduction, Nanoscale 10 (2018) 21076–21086, https://doi.org/10.1039/c8nr06538a.

[41] X. Lu, D. Wang, L. Ge, L. Xiao, H. Zhang, L. Liu, J. Zhang, M. An, P. Yang, Enriched graphitic N in nitrogen-doped graphene as a superior metal-free electrocatalyst for the oxygen reduction reaction, New J. Chem. 42 (2018) 19665–19670, https://doi.org/10.1039/c8nj04857f.

[42] C. Xuan, B. Hou, W. Xia, Z. Peng, T. Shen, H.L. Xin, G. Zhang, D. Wang, From a ZIF-8 polyhedron to three-dimensional nitrogen doped hierarchical porous carbon: an efficient electrocatalyst for the oxygen reduction reaction, J. Mater. Chem. A 6 (2018) 10731–10739, https://doi.org/10.1039/c8ta02385a.

[43] J. Han, X. Meng, L. Lu, J. Bian, Z. Li, C. Sun, Single-atom Fe-Nx-C as an efficient electrocatalyst for Zinc–air batteries, Adv. Funct. Mater. 29 (2019), 1808872, https://doi.org/10.1002/adfm.201808872.

[44] J. Wang, G. Han, L. Wang, L. Du, G. Chen, Y. Gao, Y. Ma, C. Du, X. Cheng, P. Zuo, G. Yin, ZIF-8 with ferrocene encapsulated: a promising precursor to single-atom Fe embedded nitrogen-doped carbon as highly efficient catalyst for oxygen electroreduction, Small 14 (2018), 1704282, https://doi.org/10.1002/smll.201704282.

[45] G. Ye, K. Zhao, Z. He, R. Huang, Y. Liu, S. Liu, Fe-N$_x$ sites enriched carbon micropolyhedrons derived from Fe-doped zeolitic imidazolate frameworks with reinforced Fe-N coordination for efficient oxygen reduction reaction, ACS Sustain. Chem. Eng. 6 (2018) 15624–15633, https://doi.org/10.1021/acssuschemeng.8b04105.

[46] Y. Deng, B. Chi, J. Li, G. Wang, L. Zheng, X. Shi, Z. Cui, L. Du, S. Liao, K. Zang, J. Luo, Y. Hu, X. Sun, Atomic Fe-doped MOF-derived carbon polyhedrons with high active-center density and ultra-high performance toward PEM fuel cells, Adv. Energy Mater. 9 (2019), 1802856, https://doi.org/10.1002/aenm.201802856.

[47] A. Liu, C. Li, X. Ren, L. Gao, T. Ma, Co loaded on graphene with interfacial structure as high performance catalyst for 4e$^-$ ORR: a DFT study, Ionics 26 (2020) 3483–3490, https://doi.org/10.1007/s11581-020-03471-2.

[48] J. Li, H. Zhang, W. Samarakoon, W. Shan, D.A. Cullen, S. Karakalos, M. Chen, D. Gu, K.L. More, G. Wang, Z. Feng, Z. Wang, G. Wu, Thermally driven structure and performance evolution of atomically dispersed FeN$_4$ sites for oxygen reduction, Angew. Chem. Int. Ed. 58 (2019) 18971–18980, https://doi.org/10.1002/anie.201909312.

[49] Z. Yang, Y. Wang, M. Zhu, Z. Li, W. Chen, W. Wei, T. Yuan, Y. Qu, Q. Xu, C. Zhao, X. Wang, P. Li, Y. Li, Y. Wu, Y. Li, Boosting oxygen reduction catalysis with Fe–N$_4$ sites decorated porous carbons toward fuel cells, ACS Catal. 9 (2019) 2158–2163, https://doi.org/10.1021/acscatal.8b04381.

[50] Y. Jia, X. Xiong, D. Wang, X. Duan, K. Sun, Y. Li, L. Zheng, W. Lin, M. Dong, G. Zhang, W. Liu, X. Sun, Atomically dispersed Fe-N$_4$ modified with precisely located S for highly efficient oxygen reduction, Nano-Micro Lett. 12 (2020) 116, https://doi.org/10.1007/s40820-020-00456-8.